

Modeling of H α Eruptive Events Observed at the Solar Limb

P. Kotrč · M. Bárta · P. Schwartz · Y.A. Kupryakov ·
L.K. Kashapova · M. Karlický

Received: 17 November 2011 / Accepted: 10 October 2012 / Published online: 6 November 2012
© Springer Science+Business Media Dordrecht 2012

Abstract We present spectra and slit-jaw images of limb and on-disk eruptive events observed with a high temporal resolution by the Ondřejov Observatory optical spectrograph. Analysis of the time series of full width at half-maximum (FWHM) in H α , H β , and radio and soft X-ray (SXR) fluxes indicates two phenomenologically distinct types of observations which differ significantly in the timing of FWHM and SXR/radio fluxes. We investigated one such unusual case of a limb eruptive event in more detail. Synthesis of all observed data supports the interpretation of the H α broadening in the sense of regular macroscopic plasma motions, contrary to the traditional view (emission from warm dense plasma). The timing and observed characteristics indicate that we may have actually observed the initiation of a prominence eruption. We test this scenario via modeling of the initial phase of the flux rope eruption in a magnetohydrodynamic (MHD) simulation, calculating subsequently – under some simplifying assumptions – the modeled H α emission and spectrum. The modeled and

Advances in European Solar Physics

Guest Editors: Valery M. Nakariakov, Manolis K. Georgoulis, and Stefaan Poedts

P. Kotrč · M. Bárta (✉) · P. Schwartz · Y.A. Kupryakov · M. Karlický
Astronomical Institute, Academy of Sciences, Ondřejov, Czech Republic
e-mail: barta@asu.cas.cz

P. Kotrč
e-mail: pkotrc@asu.cas.cz

M. Karlický
e-mail: karlicky@asu.cas.cz

P. Schwartz
Astronomical Institute, Slovak Academy of Sciences, Tatranská Lomnica, Slovakia
e-mail: pschwartz@ta3.sk

Y.A. Kupryakov
Sternberg Astronomical Institute, Moscow University, Moscow, Russia
e-mail: kupry@asu.cas.cz

L.K. Kashapova
Radioastrophysical Department, Institute of Solar-Terrestrial Physics, Irkutsk, Russia
e-mail: lk@iszf.irk.ru

observed data correspond well. Nevertheless, the following question arises: To what extent is the resulting emission sensitive to the underlying model of plasma dynamics? To address this issue, we have computed a grid of kinematic models with various arbitrary plasma flow patterns and then calculated their resulting emission. Finally, we suggest a diagnostics based on the model and demonstrate that it can be used to estimate the Alfvén velocity and plasma beta in the prominence, which are otherwise hard to obtain.

Keywords Flares · Eruptions · Spectrum · MHD · Models · Chromosphere · Radio flux

1. Introduction

Physical processes in a flare plasma manifest themselves in the profiles of chromospheric emission lines. As flares are very dynamic phenomena, any substantial and resolvable change of principal plasma parameters along the line of sight (LOS), *e.g.*, density, temperature, microturbulence, flowing plasma velocity component, splitting or merging plasma loops, *etc.*, has an influence on the line profiles. From individual emission profile parameters, such as the maximum intensity, Doppler width and Doppler shift, bisector, asymmetry, and total width of the line, useful quantitative and qualitative information can be derived.

Among these parameters, the full width at half maximum (FWHM) has been used as a principal parameter since the time when the spectra of solar flares began to be observed systematically; see Švestka and Fritsová (1956) and Švestka (1976), and references therein. The H α line width has been used as one of the quantitative parameters for solar flare importance. Basically, the width of the emission line is proportional to the number of radiating atoms in the flare but can be substantially altered by the presence of microturbulence or even macroscopic motions along the LOS. Changes and dynamics of the line width of H α and other lines during the time of observation and in various locations can thus be used for the study of plasma processes in a flare.

Dynamic, broad-line H α emission features observed during solar flares have been traditionally ascribed to excited chromospheric plasmas, in which both the temperature and density are enhanced due to the bombardment by energetic particles accelerated in the reconnection site higher in the corona (chromospheric evaporation and heating). Nevertheless, not all observations fit this scheme. In particular, some limb eruptive events call for another interpretation.

In this article we start by combining the H α FWHM time profile with the time evolution of radio and X-ray fluxes. The correlation of those series can differ for different flares, and we did find two phenomenologically distinct types of spectroscopic observations (see below). This indicates that different processes are behind (at first glance) the similar observed feature: the line broadening. We aim to identify those unknown processes by interpreting the results of our analysis of the observed data. While one type of broad-line emission features can be interpreted in terms of the traditional view as a chromospheric response to particle beam bombardment, the second one, exhibiting unusual timing of the H α FWHM signal, calls for a different explanation. Analyzing the available data for one such particular case we conjecture that the unusual dynamics in the H α line profile is due to macroscopic motions in the magnetic flux rope which just starts to erupt (see, *e.g.*, Lin and Forbes, 2000; Török and Kliem, 2005; Kliem and Török, 2006; Williams *et al.*, 2005; Kliem *et al.*, 2010, and references therein). H α emission from the erupting prominence material can be observed just in the case of limb events when we, in contrast, do not observe the later-occurring emission from flare ribbons that are in limb events strongly decreased by the projection effect or even completely occulted.

After assuming this working hypothesis, a numerical magnetohydrodynamic (MHD) model is used to calculate the dynamics of the magnetized plasmas. Its results are subsequently utilized as input data in simplified calculations of the H α emission; we model both the filtergram-like image and the spectral line. In order to test the sensitivity of plasma flow models to resulting observable features a grid of kinematic models of plasma flows have been also calculated and their emission characteristics (again, image and spectrum) constructed. Finally, the MHD model, in conjunction with the observations, is used for estimation of plasma parameters that are otherwise hard to obtain, like the local Alfvén speed and plasma beta in the observed structure.

The article is organized as follows. First, the observations and their analysis are presented in Section 2. Based on the observed data, a tentative hypothesis is adopted and incorporated into a numerical MHD model in Section 3. The model results are further processed to obtain final outputs that can be compared with observations: modeled image and spectral line (Section 4). In Section 5 we compare the modeled and observed data and we estimate the sensitivity of the modeled observable emission to the underlying model of the plasma flow. We also discuss the possibility of utilizing the MHD model for plasma diagnostics. Finally, the main results are summarized in Section 6.

2. Observation and Analysis

We use flare observations performed by the Ondřejov *Multichannel Flare Spectrograph* (MFS) as a primary dataset for our analysis. The instrument is continuously upgraded – for its early history see Valníček *et al.* (1959). By the time of the observations described in the current article the detectors have been replaced by video cameras, the camera objective optical system has been changed, and the slit-jaw system has been implemented as described in Kotrč (1997). We simultaneously observed the flare spectra in the H α , H β , and CA II 8542 Å lines, and also took simultaneous H α slit-jaw images (filtergrams). Both the spectra and images were recorded with a cadence of 25 images per sec.

The flare spectra have been obtained with a theoretical spatial resolution of 1 arcsec, but practically, of 3 arcsec, due to seeing degradation during the observation of the flares. The spectral resolution is about 40 mÅ in H α , and about 30 mÅ in H β . The resolution values refer to the width of one pixel. In this paper we analyze H α spectrograms and filtergrams only, as the emission in this line is the most intense for all the studied flares.

We selected four flares in total for our analysis, two on the solar disk and two on the limb. The selection was constrained by the requirement that the observations cover the entire flare evolution from its very beginning. All the flares are of observationally different types and of different importance. In this paper we present a comparative analysis for one disk-center and one limb event. The other two flares show qualitatively the same behavior for their respective category (limb and disk center).

Figure 1 shows an on-disk flare that occurred on 5 August 2003 at 09:07–09:23 UT (maximum at 09:14 UT) in AR NOAA 10421 located S05 W34. Its X-ray class was C3.5 according to *Geostationary Operational Environmental Satellite* (GOES) data. Panel (a) shows the H α image taken by the solar patrol of the Ondřejov Observatory, panel (b) shows the slit-jaw image of the flare, and the simultaneously taken H α spectrum is shown in panel (c).

The 4 August 2002 solar flare occurred from 08:58 UT to 10:33 UT (maximum at 09:55 UT) in AR NOAA 0050, just at the western limb. The flare was classified as M6.6 according to GOES. For the Ondřejov solar patrol H α image and the MFS spectrum and slit-jaw image, see Figure 2.

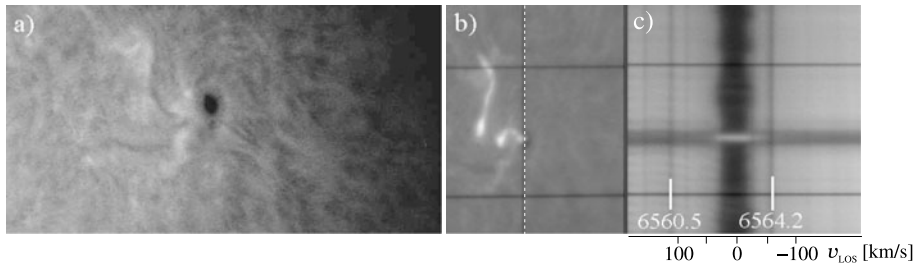


Figure 1 Observations of the on-disk event on 5 August 2003. (a) $H\alpha$ solar patrol image (Ondřejov Observatory) shows AR NOAA 0421 with a large sunspot before the flare (at 05:56:10 UT); (b) $H\alpha$ slit-jaw image observed at 09:05:46 UT by MFS (the vertical dashed line indicates the slit position); (c) simultaneously observed MFS $H\alpha$ spectrum. The vertical lines in the spectrum record are marked by the wavelengths in ångströms; the corresponding Doppler velocity scale is shown on the axis below.

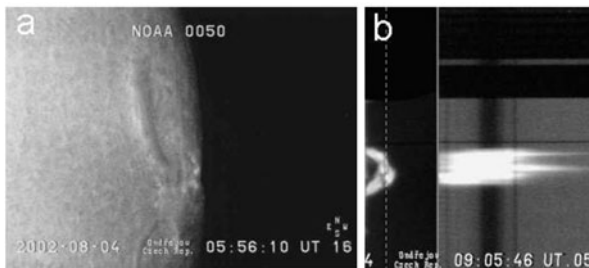


Figure 2 Observation of the limb event on 4 August 2002. (a) $H\alpha$ solar patrol image (Ondřejov Observatory) showing the AR crossing the western limb; (b) MFS image composed from left to right of $H\alpha$ slit-jaw and the simultaneously taken $H\alpha$ spectrum with a broad emission. The number after UT is the frame number in the series of 25 frames taken in one second.

For each event we analyzed the $H\alpha$ line profiles along the slit and searched for maximum FWHM. This value was selected to obtain the time series of the FWHM representative of the source as a whole. The standard scenario assumes that the $H\alpha$ emission comes from the plasma excited in the process of chromospheric evaporation and heating by the energy deposited in the chromosphere by energetic electrons accelerated higher in the corona. Therefore, it is meaningful to make a correlation analysis between the $H\alpha$ FWHM and the soft X-ray (SXR) and decimetric (microwave, MW) radio signals that reflect the plasma heating and propagation of energetic electrons through the lower corona, respectively. Such correlation analyses are useful for understanding the processes of accelerated-particle energy deposition in the chromosphere and the chromospheric radiative response in optical lines. Hence, we compared the obtained $H\alpha$ FWHM time series with temporal profiles of the SXR data from GOES-12, 1–8 Å (<http://spidr.ngdc.noaa.gov/spidr/dataset.do>) and the radio flux measured by the Ondřejov RT3 radio telescope at 3 GHz (<http://www.asu.cas.cz/~radio/>). The results of this analysis are displayed in Figure 3. Figure 3a shows the correlation of these three signals for the on-disk event on 5 August 2003. At the very beginning of the flare we can see a gradual X-ray flux rise; then microwaves (MW) at 3 GHz and the $H\alpha$ line FWHM begin to rise simultaneously. The slopes of all three normalized curves are practically identical. To sum up, for the flare of 5 August 2003 we see a very synchronized rise of all three curves.

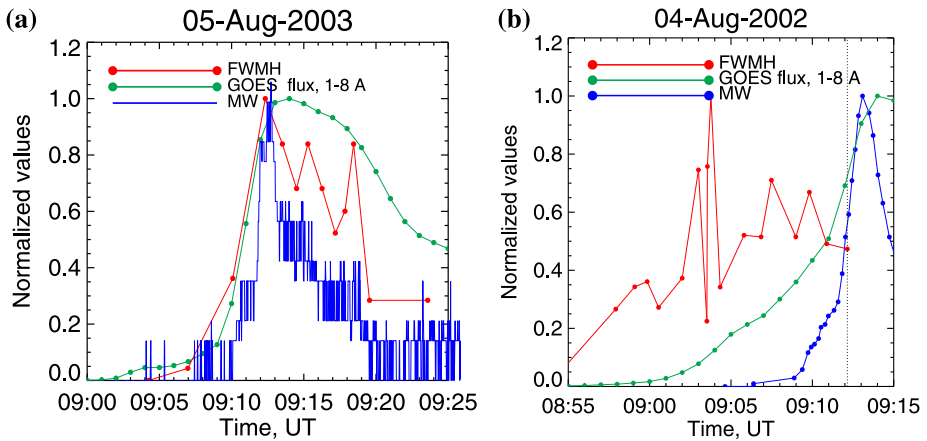


Figure 3 Time profiles of microwave (MW) radio flux at 3.0 GHz and GOES flux (channel 1–8 Å) compared with FWHM as measured in H α emission line during a flare on the solar disk (a) and a limb flare (b). The time profiles are normalized to their peak values within the studied time interval.

However, in Figure 3b, which displays the same kind of analysis for the 4 August 2002 event, we see a quite different behavior. The maximum FWHM value of ≈ 10 Å was detected at 09:04 UT, *i.e.*, quite a long time before the flare maximum at both SXR and MW, the latter two being more or less synchronous. While the on-disk event (Figure 3a) fits well into the standard scenario, which ascribes broad H α line emission to dense plasmas excited as a consequence of particle beam energy deposits, the line broadening during the selected limb event (Figure 3b) is most likely produced by a different physical mechanism. We will now analyze that event in more detail.

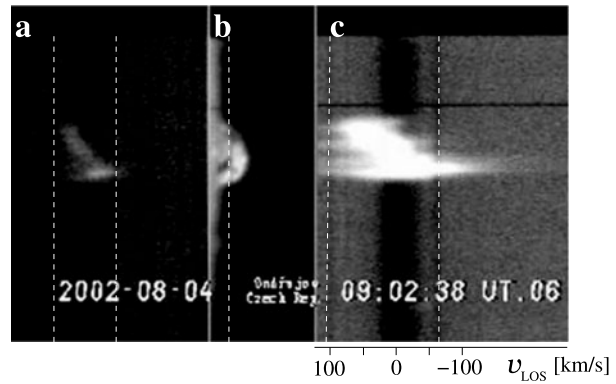
2.1. Analysis of 4 August 2002 Limb Eruption

The unusual timing of the H α FWHM time profile with respect to SXR and MW radio flux calls for another explanation of the enhanced H α for the studied event of the 4 August 2002 limb eruption. To obtain insight into the physical mechanisms causing strong broadening of the line emission well in advance of the beginning of the X-ray flare we accumulated a set of further observational data related to the studied event.

In addition to the H α line, the flare has also been observed in other spectral channels recorded in the MFS. Figure 4 shows a combination of the H α slit-jaw image (b) and simultaneous spectral observations in H β (a) and H α (c). The line profile in H β is also strongly broadened and exhibits similar qualitative features to those of H α , but the signal is substantially weaker. Nevertheless, observation at this time (09:02:38 UT) also shows that the total line broadening is most likely formed by stacking of more narrow-line contributions with different Doppler velocities from different positions along the slit (*y*-axis). Here the Doppler shifts of the individual components exceed their line broadenings, revealing the composed nature of the broad-line emission (see the “tilt” of the line-profile distribution along the slit in Figure 4). This is less obvious at later times in the event (see Figure 2). Hence, the observation indicates a significant role of macroscopic motions for the line formation.

Taking into account the H α FWHM timing observed in our analysis, the following tentative hypothesis can be assumed. Since the largest spectral line broadening/distortion precedes the flare onset in SXRs, we most likely observe signatures of the plasma motions in

Figure 4 Ondřejov MFS image composed of H β spectrum (a), H α slit-jaw filtergram (b), and H α spectrum (c) for the 4 August 2002 limb eruption. The spectra show the most typical feature for the limb events: the tilt of the spectral line profile along the slit.



the pre-event structure, which we assume to be a magnetic flux rope (prominence/filament). These motions can be caused by an MHD instability that developed in the flux rope after its threshold was reached. However, the pre-instability phase related to, *e.g.*, helicity injection into the flux rope due to vortex driving in its feet can also lead to the rope deformations and consequent observed plasma motions.

Flux rope eruptions via, for example, a kink or torus instability – see, *e.g.*, Török and Kliem (2005), Williams *et al.* (2005), or Kliem *et al.* (2010) – are nowadays a key aspect of the standard flare scenario (see, *e.g.*, Magara *et al.*, 1996 and Shibata and Tanuma, 2001, and references therein). The eruptions are usually preceded by a slow rise of the filament, generally described as “filament activation.” This phase may correspond to helicity injection into the flux rope and consequent motions. If enough twist is accumulated in the rope, a helical kink instability can develop as shown by Kumar *et al.* (2012). A similar effect in highly twisted flux ropes can be seen in simulations by Kliem *et al.* (2010). Only later does the exponential rise of the filament take place, connected with the impulsive phase of the associated flare.

Should the above interpretation be correct, a coronal mass ejection (CME) formed at later stages from the erupted flux rope will be seen. Indeed, combined observations from the *Solar and Heliospheric Observatory* (SOHO) *Extreme Ultraviolet Imaging Telescope* (EIT) and C2 coronagraph show signatures of CME ejection in the studied region (see Figure 5).

Further inspection of the data has shown that the studied flare on 4 August 2002 represents a long-duration event. This can be seen in time profiles of GOES data (Figure 6). As the X-ray profiles show, the flare starting at $\approx 09:10$ UT was followed by a subsequent event starting at $\approx 14:00$ UT.

An interesting feature can also be seen in radio spectra. Figure 7 shows the radio spectrum from the *Phoenix-2* spectrograph at Eidgenössische Technische Hochschule (ETH) Zurich, also known as the Swiss Federal Institute of Technology (<http://soleil.i4ds.ch/solarradio/>). The dominant structure here is the radio continuum starting around 09:10 UT. This emission is preceded by a weak microwave type III burst at $\approx 09:04$ UT (marked by an arrow), which indicates the presence of accelerated electrons even in this very early stage of the event. Both bursts are limited to the higher frequency range (> 1.5 GHz). Assuming the plasma emission as a preferred radiation mechanism, this indicates that the radio source has been bound to the lower solar atmosphere. The same features are present in the radio spectra observed by the Ondřejov RT4 spectrograph. We will return to these facts later in Section 5.

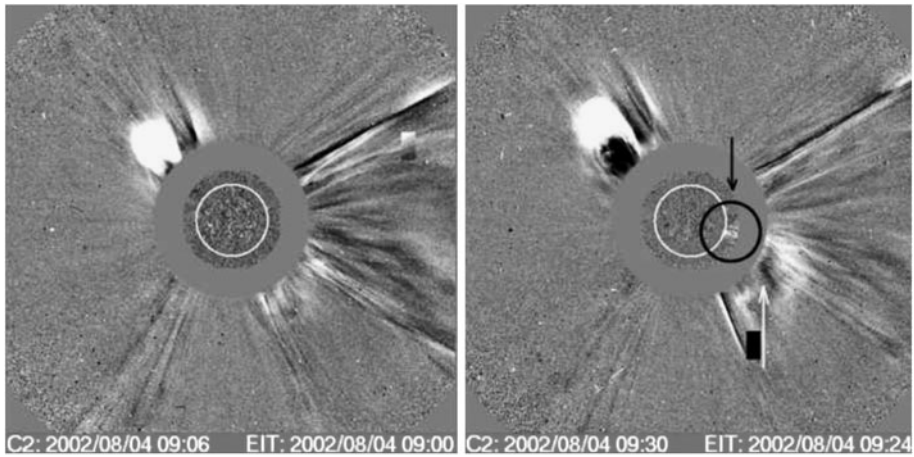
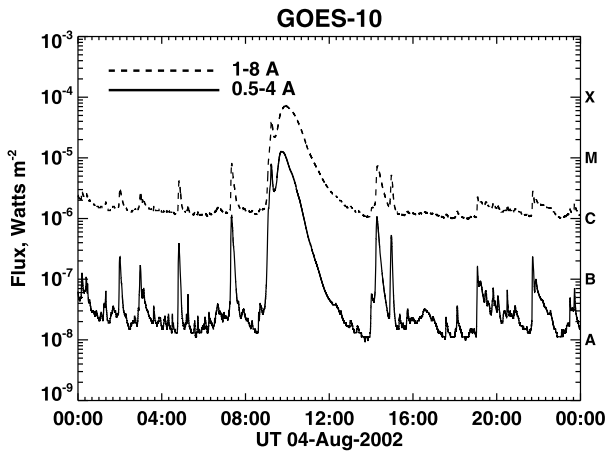


Figure 5 Combined SOHO/EIT and SOHO/LASCO/C2 difference images observed on 4 August 2002 at 09:00 UT just at the flare onset (left). The image to the right obtained at 09:24 UT shows the emission feature in the dark circle connecting the studied active region with the CME signature marked by the white arrow.

Figure 6 Time plot of GOES-10 shows a long-duration flare starting at \approx 09:10 UT.



3. MHD Model

In the previous section we assumed a tentative hypothesis to interpret the 4 August 2002 limb event. Based on the analysis of the observed data, we interpret the strong line broadenings seen well in advance of the flare maximum as an effect of macroscopic motions in a magnetic flux rope at the very beginning of its eruption. Here we implement this idea into a numerical MHD model.

The large-scale evolution of magnetized plasma can be adequately described by a set of compressible resistive one-fluid MHD equations (see, *e.g.*, Priest, 1984):

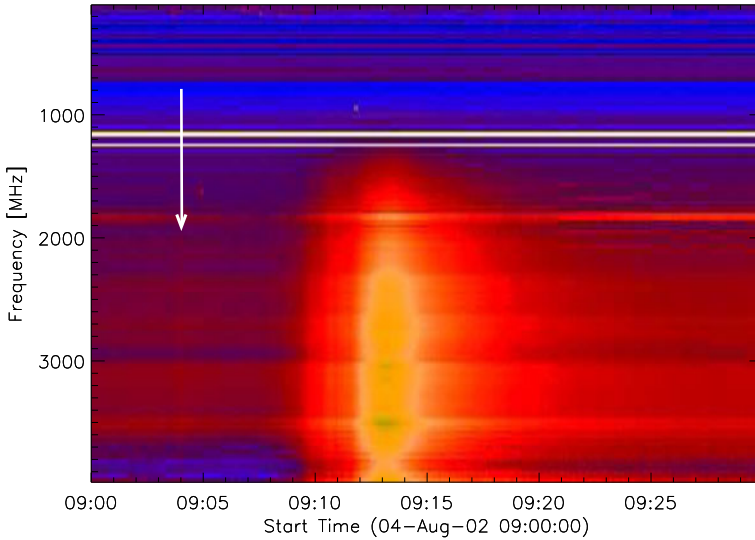


Figure 7 Radio spectrum from Phoenix-2 spectrograph at ETH Zurich. Decimetric type III burst at 09:04 UT (indicated by arrow) is followed by continuum radio emission.

$$\begin{aligned}
 \frac{\partial \rho}{\partial t} + \nabla \cdot (\rho \mathbf{u}) &= 0 \\
 \rho \frac{\partial \mathbf{u}}{\partial t} + \rho (\mathbf{u} \cdot \nabla) \mathbf{u} &= -\nabla p + \mathbf{j} \times \mathbf{B} + \rho \mathbf{g}, \\
 \frac{\partial \mathbf{B}}{\partial t} &= \nabla \times (\mathbf{u} \times \mathbf{B}) - \nabla \times (\eta \mathbf{j}), \\
 \frac{\partial U}{\partial t} + \nabla \cdot \mathbf{S} &= \rho \mathbf{u} \cdot \mathbf{g}.
 \end{aligned}
 \tag{1}$$

The set of Equations (1) is to be solved by means of the second-order leapfrog finite volume method (FVM). For the numerical solution it is first rewritten in its conservative form. The (local) state of the magnetofluid is then represented by the vector of basic variables $\Psi \equiv (\rho, \rho \mathbf{u}, \mathbf{B}, U)$, where ρ , \mathbf{u} , \mathbf{B} , and U are the plasma density, plasma velocity, magnetic field strength, and total energy density, respectively (see Bárta, Karlický, and Žemlička, 2008; Bárta, Vršnak, and Karlický, 2008, and Bárta *et al.*, 2011a for details). The energy flux \mathbf{S} is calculated as

$$\mathbf{S} = \left(U + p + \frac{B^2}{2\mu_0} \right) \mathbf{u} - \frac{(\mathbf{u} \cdot \mathbf{B})}{\mu_0} \mathbf{B} + \frac{\eta}{\mu_0} \mathbf{j} \times \mathbf{B},
 \tag{2}$$

and the auxiliary variables, plasma pressure p and current density \mathbf{j} , are implicitly defined by the relations

$$\begin{aligned}
 \nabla \times \mathbf{B} &= \mu_0 \mathbf{j}, \\
 U &= \frac{p}{\gamma - 1} + \frac{1}{2} \rho u^2 + \frac{B^2}{2\mu_0},
 \end{aligned}$$

where \mathbf{g} is the gravity acceleration, taken to be uniform and approximated by its value at the photospheric level.

We are interested in the very beginning phases of a flux rope eruption, because in the observed (slit-jaw) image data we see neither significant changes in the observed structure nor signatures of plasma ejections – the entire structure remains confined in a rather small volume during the time interval of our analysis (08:55 – 09:12 UT). However, at later stages, the prominence fully erupts, and we can see only its remaining legs in the rather narrow field of view provided by the slit-jaw imaging system. For this reason we suppose that intense small-scale current sheets (CSs) are not developed yet via the cascade of current-density fragmentations in our time interval of interest (Bárta *et al.*, 2011a, 2011b; Karlický and Bárta, 2011); consequently, the effects of anomalous (generalized) resistivity do not take place at this stage of the evolution. Hence, we limit ourselves to the ideal MHD, setting the (generalized) resistivity $\eta = 0$ everywhere.

We model the flux rope at its initial state as follows: For the magnetic field we assume the model by Titov and Démoulin (1999), which describes a twisted (*i.e.*, current-carrying) flux rope as part of a torus with minor and major radii a and R , and winding number N_t , respectively. The magnetic configuration is kept in a global equilibrium by the action of the Lorentz force due to the overlying magnetic field. The sources of this “ambient” field are modeled by a subphotospheric line current I_0 and a pair of magnetic charges $+q, -q$, all located at the major axis of the torus. We shall now describe the model in more detail.

First of all, in numerical simulations, it is frequently convenient to express variables in their natural units (see, *e.g.*, Kliem, Karlický, and Benz, 2000). Thus, we express the spatial coordinates in the units of the flux rope (torus) minor radius a , the magnetic field strength in terms of the magnetic field at the surface of the torus B_o , and time in units of the Alfvén transit time over the unit length a , *i.e.*, $\tau_A = a/V_{A,0}$, where $V_{A,0} = B_o/\sqrt{\mu_o\rho_o}$ is the Alfvén speed calculated at the torus surface with the density corresponding to its value inside the torus at the bottom of the simulation box (see below). Consequently, all velocities are also expressed in terms of the Alfvén speed $V_{A,0}$.

In this dimensionless set of units, which we will use from now on, the magnetic field components of the Titov–Démoulin model (1999) can be described as

$$\mathbf{B}_{in} = \left(\sqrt{1 + 2\left(\frac{N_t}{R}\right)^2 (1 - r^2)} + \frac{R}{r_\perp} - 1 \right) \hat{\boldsymbol{\theta}} + \nabla \times \left(N_t \sqrt{\frac{1}{Rr_\perp}} \left[A(k_a) + \left. \frac{dA(k)}{dk} \right|_{k_a} (k - k_a) \right] \hat{\boldsymbol{\theta}} \right) + q \left(\frac{\mathbf{r}_+}{|\mathbf{r}_+|^3} - \frac{\mathbf{r}_-}{|\mathbf{r}_-|^3} \right) \quad (3)$$

for the field inside the torus, and

$$\mathbf{B}_{ext} = \frac{R}{r_\perp} \hat{\boldsymbol{\theta}} + \nabla \times \left(N_t \sqrt{\frac{1}{Rr_\perp}} A(k) \hat{\boldsymbol{\theta}} \right) + q \left(\frac{\mathbf{r}_+}{|\mathbf{r}_+|^3} - \frac{\mathbf{r}_-}{|\mathbf{r}_-|^3} \right) \quad (4)$$

for the external region. Here, r denotes the distance from the torus minor axis (denoted as ρ in Titov and Démoulin, 1999, which conflicts with the designation for density in our paper). All other symbols keep their meaning from the paper by Titov and Démoulin (1999), the length-like quantities now being expressed in the torus minor radius a .

The condition for global equilibrium (Equation (6) in Titov and Démoulin, 1999) reads in our dimensionless units as

$$B_{q,0} = \frac{\ln(8e^{-5/4}R)}{2R^2} N_t$$

where

$$B_{q,0} = \frac{2q}{R^2} \left(\frac{R}{L}\right)^2 \left[1 + \left(\frac{R}{L}\right)^2\right]^{-3/2}$$

is the magnetic field strength caused by the pair of magnetic charges, separated by distance $2L$, at the minor axis of the torus ($r_{\perp} = R$). Consequently, for the magnetic charge in a globally balanced configuration, we obtain

$$q = \frac{\ln(8e^{-5/4}R)}{4} N_t \left(\frac{R}{L}\right)^{-2} \left[1 + \left(\frac{R}{L}\right)^2\right]^{3/2}. \tag{5}$$

Thus, we have four free parameters in the model: the torus major radius R (expressed in units of minor radius a), the ratio between magnetic charge separation and the torus major radius R/L (which controls the stability of the equilibrium – see Appendix A in Titov and Démoulin, 1999), the winding number N_t , and the geometrical factor d , which controls how deep the whole structure is submerged into the photosphere. In our simulation we use the following values: $R = 3.0$, $L/R = 0.5$, $d = 0.5R$, and $N_t = 5$.

The entire magnetic structure is filled with plasma. Because of the presence of gravity in our model, we use a stratified density structure according to the relations

$$\rho_{\text{in}} = \rho_0 \exp\left(-\frac{z}{\frac{T_{\text{ext}}}{T_{\text{in}}} L_G}\right) \tag{6}$$

and

$$\rho_{\text{ext}} = \frac{T_{\text{in}}}{T_{\text{ext}}} \rho_0 \exp\left(-\frac{z}{L_G}\right) \tag{7}$$

for the torus (flux rope/filament) interior and external space (corona), respectively. In our dimensionless variables we set $\rho_0 = 1$. Here L_G is the gravity height scale in the corona; $L_G = 2k_B T_{\text{ext}}/(m_p g)$ for fully ionized hydrogen plasma. The temperature ratio between coronal (hot) and flux rope (warm) plasmas has been chosen as $T_{\text{ext}}/T_{\text{in}} = 10$. This value represents a compromise between a more realistic ratio (≈ 100) and the stability of the code; the latter is always challenged by high gradients, particularly in combination with limited spatial resolution.

The coronal height scale L_G introduces natural scaling for our simulation. For a typical coronal temperature $T_{\text{ext}} = 2 \times 10^6$ K it reaches a value $L_G = 1.2 \times 10^8$ m. Since we use $L_G = 20$ in our dimensionless units, the torus minor radius (the unit of length) corresponds to $a = 6000$ km in SI units. The apex of the structure is then at a height of (SI units) $h_a \approx (R - d)a + a = 15000$ km. This roughly corresponds to the observation in the slit-jaw filtergram.

The density stratification according to Equations (6) and (7) ensures that $\nabla \mathbf{p}$ compensates the gravity locally in the internal and external domain. Also, the magnetic field described by Equations (3) and (7) is (approximately) force-free ($\mathbf{j} \times \mathbf{B} \approx \mathbf{0}$). Thus, only the different height scales $L_{G,\text{ext}} \equiv L_G$ and $L_{G,\text{int}} = L_G T_{\text{int}}/T_{\text{ext}}$ result in some components of $\nabla \mathbf{p}$ at the boundary between the flux rope and its surroundings. As we use a low plasma beta in our simulations ($\beta = 0.05$ at $z = 0$ and $t = 0$) and the total height of our domain is – in line with observations of the 4 August 2002 event – only a fraction of the coronal height scale, the departure from equilibrium is small and does not affect the dynamics significantly.

The calculation is performed in a 3D numerical box of size $100 \times 200 \times 100$ grid cells in the x , y , and z directions; see Titov and Démoulin (1999) for a definition of the reference frame. The spacing is equidistant: $\Delta x = \Delta y = \Delta z = 0.044$. We use a driven boundary

condition at the bottom boundary simulating helicity injection due to (sub)photospheric motions. It is implemented by a velocity field (at $z = 0$) of the following form:

$$\begin{aligned} u_x(x, y, 0, t) &= -\omega(t)\varepsilon[(y - y_1)w_1(x, y) + (y - y_2)w_2(x, y)], \\ u_y(x, y, 0, t) &= \omega(t)\frac{1}{\varepsilon}[xw_1(x, y) + xw_2(x, y)], \end{aligned} \tag{8}$$

where the vorticity functions $w_1(x, y)$ and $w_2(x, y)$ describing the rotational motions around the footpoint centers $[x_i, y_i]$, $i \in \{1, 2\}$ (i.e., the points, where the axis of the flux rope (i.e., torus minor axis $r_\perp = R$) crosses the bottom boundary) are expressed as

$$w_i(x, y) = \frac{1}{2}\left[1 + \tanh\left(\frac{1 - \bar{r}_i}{\Delta}\right)\right]. \tag{9}$$

Here, the projection-corrected distance from the footpoint centers 1 and 2 is

$$\bar{r}_i = \sqrt{\varepsilon^2(y - y_i)^2 + x^2}, \tag{10}$$

and $\Delta = 0.1$ so the velocity gradient is resolved by five cells. Finally, the projection factor ε and the y coordinates of footpoint centers y_1 and y_2 (note that $x_1 = x_2 = 0$) are found from simple geometrical considerations in the forms

$$\varepsilon = \sqrt{1 - \left(\frac{d}{R}\right)^2} \tag{11}$$

and

$$y_{1,2} = \pm\varepsilon R. \tag{12}$$

The boundary condition at $z = 0$ can be understood as follows. Equations (8)–(12) basically describe vortex motions (with the same orientation), localized in the (approximately elliptical) cross-sectional areas of the torus with the bottom boundary $z = 0$, around the footpoint centers. The rotation is oriented such that it leads to an increase of the magnetic twist in the rope. If the submerge distance d were equal to zero, i.e., if exactly half of the torus were above the photosphere, the velocity pattern would look like two circular plates with solid-state rotation surrounded by plasmas which remain at rest. The transition between moving and rest plasmas is described by a Fermi–Dirac-like distribution for normalized angular velocity on the distance from the footpoint center; see Equation (9). However, this is not the case. The torus is actually submerged by $d = 0.5R$ in our case, and therefore purely geometrical projection factors must be taken into account. This is why the formulae are modified by the factor ε .

The parameter $\omega(t)$ describes the magnitude of the angular velocity. We have chosen its gradual increase followed by a constant value according to the relation

$$\omega(t) = \frac{\omega_0}{2}\left[1 + \tanh\left(\frac{t - t_{\text{drive}}}{t_{\text{ramp}}}\right)\right]. \tag{13}$$

First, we let the system relax for a short time, until $t_{\text{drive}} = 2.0$, in order to clean $\nabla \cdot \mathbf{B}$, which is not exactly zero as there still exists a small mismatch between the internal and external magnetic fields described by the Titov–Démoulin (1999) model in Equations (3) and (4). Then, the angular velocity is gradually increased, during the period lasting $2t_{\text{ramp}} = 2.0$. Eventually, the angular velocity reaches its plateau at $\omega_0 = 0.3$, which corresponds to a maximum photospheric driving velocity at the level of $\approx 10\%$ of the Alfvén speed in the ambient corona.

The remaining quantities at the bottom boundary $z = 0$ fulfill the following boundary conditions: $u_z(x, y, 0, t) = 0$, $\partial\rho/\partial z|_{(x,y,0,t)} = -\rho/L_G$, $\partial p/\partial z|_{(x,y,0,t)} = -p/L_G$, $\partial B_x/\partial z|_{(x,y,0,t)} = \partial B_y/\partial z|_{(x,y,0,t)} = 0$. The component B_z is subsequently calculated to preserve the Maxwell law $\nabla \cdot \mathbf{B} = 0$ at $z = 0$, and the total energy density U according to the spatial changes of kinetic, magnetic, and internal energies. See Bárta *et al.* (2011a) for a detailed discussion on this issue.

All other boundaries are implemented as free prescribing the von Neumann boundary condition $\partial/\partial \mathbf{n} = 0$ for \mathbf{u} and the tangent components of the magnetic field. The density and pressure respect gravity stratification: $\partial\rho/\partial \mathbf{n} = \rho \mathbf{n} \cdot \mathbf{g}/(|\mathbf{g}|L_G)$, and the same applies for p ; the normal magnetic field component and total energy density are handled similarly to the bottom boundary.

The calculations are run in the time interval $t \in \langle 0; 20 \rangle$, the time step being adaptively changed according to the Courant–Friedrichs–Levy (CFL) condition.

We present the results of our simulation in the next section.

4. Results

The results of the MHD model are displayed in Figure 8. Panels (a) through (d) show selected time frames of the magnetic field (the lines) and plasma density (background color scale) in two viewing angles: top view (left) and side view (right). As the helicity is injected into the flux rope, a sigmoidal structure is consecutively formed (visible in top view) with the flux rope legs moving oppositely in the x direction (*i.e.*, the direction perpendicular to the initial plane of symmetry of the torus). Thus, the whole structure slowly rotates around the z -axis. At the same moment, there is little torsional motion with respect to the minor torus axis $r_\perp = R$. We will now use the obtained flow pattern and density structure to estimate the $H\alpha$ emission from this model structure.

4.1. Emission Estimation

In order to obtain an output that can be directly compared with observations, we use the results of the underlying MHD model as an input for approximate calculations of $H\alpha$ emission. In general, correct calculations of the hydrogen line emission from prominences is a complicated procedure and should be performed via non-local thermodynamic equilibrium (non-LTE) radiative transfer computations, taking the nonuniform (thread-like) distribution of the plasma into account (see, *e.g.*, Heinzel and Anzer, 2001 and Gunár, Heinzel, and Anzer, 2011). In our modeling we do not aim at such detailed calculations of spectral line profiles. We would rather address the simple question of whether the underlying MHD model of the initial flux rope eruption is capable of reproducing observed filtergram images and spectra qualitatively, *i.e.*, whether robust characteristics of the spectral line like central wavelength and the width are comparable for modeled and observed emissions.

As our tentative hypothesis assumes that the line broadening is the result of the summation of rather narrow-line contributions from different lumps of plasma along the line of sight (LOS) with different Doppler velocities, we suppose optically thin emission on the given frequency channel. Thus, we can estimate the spectral image intensity $I_\nu(x, y, \nu)$ from the pixel $[x, y]$ in the Doppler velocity channel ν in arbitrary units as

$$I_\nu(x, y, \nu) = C \int_{-\infty}^{+\infty} \rho^2(x, y, z) \exp\left(-\frac{[\nu - u_z(x, y, z)]^2}{2v_T^2}\right) dz. \tag{14}$$

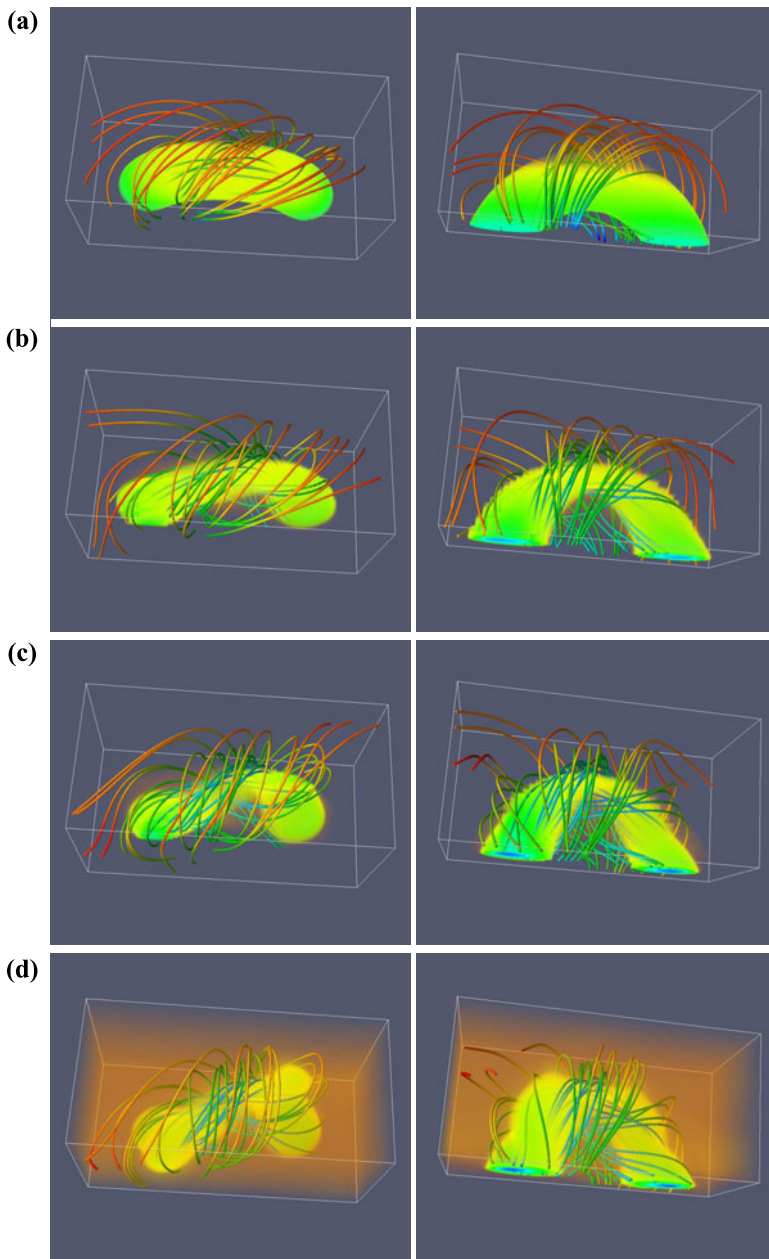


Figure 8 MHD model of the initial phase of a flux rope eruption. Thick colored lines represent magnetic field lines; their colors correspond to the local value of $|\mathbf{B}|$ (lower to higher values of $|\mathbf{B}|$ being coded from red to blue). The background color scale with varying opacity represents plasma density. Frames (a)–(d) were taken at $t = 0$ (the initial state), $t = 5.4$, $t = 11$, and $t = 14$, respectively. Top and side views are shown for each time frame.

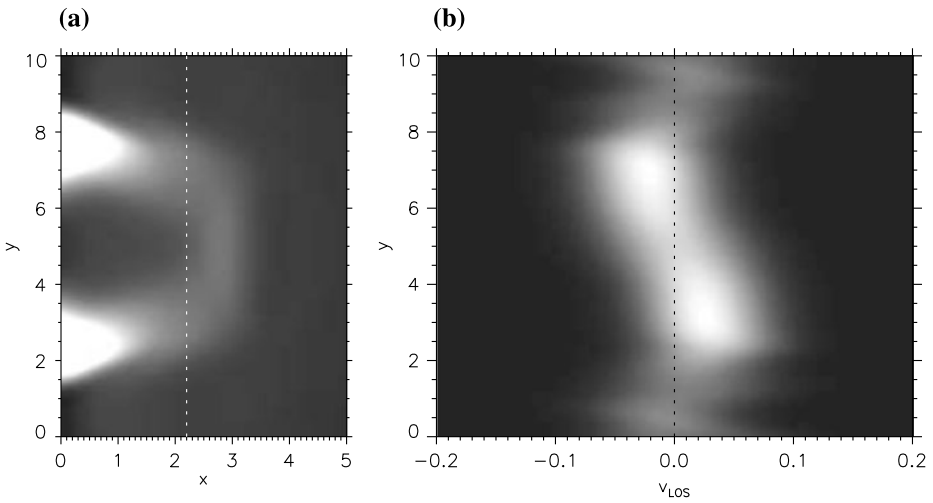


Figure 9 $H\alpha$ emission calculated from the results of the underlying MHD model at $t = 11$. (a) Modeled $H\alpha$ filtergram (to be compared with the observed slit-jaw image in Figure 4b). The vertical dashed line shows the position of the simulated spectrograph slit. (b) Modeled spectral line along the slit (to be compared with the spectral line observations in Figure 4a and c). The LOS (Doppler) velocities are expressed in terms of $V_{A,0}$. The dashed vertical line corresponds to the line center in the rest frame ($v = 0$).

Note that the reference frame has changed here. Since we wish to fit the model to the observation of the 4 August 2002 limb event (which is viewed from the side), we use a rotated Cartesian system with the z -axis now coaligned with the LOS, and the x - and y -axes corresponding to the horizontal and vertical directions in the simulated filtergram image, respectively; see Figure 9. The relations between the old coordinates used in the MHD model and the new coordinate system are simple: $x = \bar{z}$, $y = -\bar{y}$, and $z = \bar{x}$, where “barred” coordinates belong to the former system. The u_z velocity component (*i.e.*, the LOS or Doppler velocity) in the new coordinate system thus corresponds to $u_{\bar{x}}$ in the system used in the MHD model.

The ρ^2 -factor in Equation (14) takes partly into account the probability of excitation of hydrogen atoms. Self-absorption is neglected (no $e^{-\tau}$ factor). The constant C is arbitrary in our qualitative model and was set to $C = 1$. For the “thermal” broadening v_T , which also includes microturbulent velocities, we adopted the value $v_T = 0.01$ (again in terms of $V_{A,0}$).

In order to fit the observed filtergram image (Figure 4b) and spectra (Figures 4a and 4c), we extract the necessary information from the spectral intensity distribution $I_\nu(x, y, \nu)$ as follows. We assume a rather broad-band $H\alpha$ filter for our simulated slit-jaw image, with box-function-like spectral transmissivity in the Doppler velocity channel ν :

$$T_\nu(\nu) = \begin{cases} 1 & : |\nu| \leq \nu_{\text{Max}}, \\ 0 & : |\nu| > \nu_{\text{Max}}, \end{cases} \quad (15)$$

where $\pm \nu_{\text{Max}}$ are the limits of the filter bandpass. Thus, the intensity $I(x, y)$ from the pixel $[x, y]$ in the filtergram image is

$$I(x, y) = \int_{-\infty}^{+\infty} I_\nu(x, y, \nu) T_\nu(\nu) d\nu = \int_{-\nu_{\text{Max}}}^{+\nu_{\text{Max}}} I_\nu(x, y, \nu) d\nu. \quad (16)$$

To emulate the spectral line image we simply put the simulated spectrograph slit at some coordinate x_{slit} and extract the spectral information from the spectral intensity distribution $I_v(x, y, v)$ along that line $x = x_{\text{slit}}$:

$$\hat{I}_v(v, y) = I_v(x_{\text{slit}}, y, v). \quad (17)$$

The results of those procedures are shown in Figure 9. Panel (a) shows the integrated intensity $I(x, y)$ according to Equation (16), panel (b) the spectral line profile $\hat{I}_v(v, y)$ along the emulated slit located at position $x_{\text{slit}} = 2.2$ (indicated by the dashed vertical line in panel (a)). The output can be directly compared with the observations in Figure 4.

5. Discussion

Broad-line emission in hydrogen spectral lines observed in solar flares is traditionally interpreted as a chromospheric response to bombardment by energetic particle beams accelerated higher in the corona (chromospheric evaporation and heating). This interpretation assumes that signatures of downward traveling electron beams (MW radio emission), plasma heating (SXR), and excitation of hydrogen plasma (H α FWHM) are roughly synchronous, exhibiting small time lags only, which can be used in turn for detailed study of propagation of electron beams, their energy deposit, and radiative response of plasmas to the particle bombardment.

In most cases we actually see this expected behavior – a clear example is the flare on 5 August 2003. Nevertheless, for some limb events the correlation analysis of time series of SXR, MW, and H α FWHM results in a different outcome. The H α FWHM curve precedes the (almost synchronous) MW and SXR curves by minutes. In the current paper we presented the flare on 4 August 2002 as an example of such events. We found the rise of FWHM in H α line ten minutes before the flare maximum in microwaves and SXRs in this particular case. The 4 August 2002 flare satisfied some criteria of event selection used by Battaglia, Fletcher, and Benz (2009). It was located nearby the solar limb, and increasing SXR flux emission preceded the detection of accelerated electrons in the event. Battaglia, Fletcher, and Benz (2009) used the hard X-ray (HXR) flux as evidence of accelerated particle presence, but we used the MW flux because of the absence of HXR data. The principal difference between the considered flare and the events studied by Battaglia, Fletcher, and Benz (2009) is the FWHM increase before the SXR emission growth that could not be explained by heating or explosive evaporation. However, the precursor of the main SXR peak might be connected with the weak decimetric type III burst (Figure 7), indicating possible internal reconnection in the flux rope (see discussion below).

Basically, the correlation analysis described above presents two types of broad-line emission features which, at first glance, were all interpreted as a flare emission. The observed features exhibit either synchronous H α FWHM, MW, and SXR fluxes, or for others, the H α curve precedes that of MW and SXR significantly.

As the observation of 4 August 2002 (and other observations of this type) does not fit into the “traditional” chromospheric response picture, we attempted to find another plausible interpretation. The H α FWHM timing seen by our correlation analysis, the specific tilted distribution of the spectral line profile along the spectrograph slit (Figure 4), a deeper look at H α slit-jaw images, and a bunch of related multiwavelength observations indicate that we actually observe the very initial phase of the eruption and the observed line broadening can be explained as a sum of many rather narrow-line contributions with different Doppler shifts. The macroscopic motions giving rise to the observed Doppler shifts

could be associated either with the prominence activation – a slow motion related to magnetic field reconfiguration due to, *e.g.*, helicity injection – or, in the later stages, with the developed helical kink instability of the magnetic flux rope (prominence/filament). However, whether or not the instability has developed, the vertical motion of the flux rope stays limited; rather its rotation around the vertical axis appears. Only later – after fully developed eruption – does it eventually evolve into a CME (Kliem and Török, 2006; Lin and Forbes, 2000). We do not see the usual line broadening due to chromospheric evaporation in the later phases because of the geometry of the event. The chromospheric emission ribbons are either behind the limb, or at least the projection factor strongly decreases the ribbon area, well below the spatial resolution of our instrument. Note that the mentioned signatures of the filament eruption (shifted broad line) should be seen in spectroscopic observations of the on-disk events as well, but this time in absorption and with lower contrast.

In order to test this tentative hypothesis we incorporate it into an MHD numerical model. We have modeled the flux rope as (part of) a torus using the analytical equilibrium found by Titov and Démoulin (1999). We filled this magnetic structure with gravity-stratified plasma. Colder and denser material resides inside the toroidal flux rope to mimic the observed properties of filaments; the hot and appropriately rarefied surrounding plasma corresponds to the solar corona. The eruption is driven by helicity injection via vortex flows in the rope foot-points at the bottom boundary. As shown in H α slit-jaw images in Figure 2, and to some extent also indicated by the high-frequency limit of simultaneous radio emission (Figure 7), the prominence observed on 4 August 2002 is in its slow-rise (or even no rise) “activation” phase during the studied interval of spectral line broadening (08:55–09:12 UT). Hence, in line with this observation of the event we simulate only the very beginning phase of the flux rope eruption. Since it is confined in a relatively small volume during the studied period of activation, we need not construct a very vertically extended (in the sense of physical lengths) numerical box; rather we can use our numerical resolution to have a better spatial coverage of the flux rope. In this way our approach differs from models by, *e.g.*, Török and Kliem (2005) and Kliem and Török (2006), who study eruption dynamics at much larger spatial and temporal scales. Moreover, we use the full set of MHD equations, and – for obvious reasons – we are also interested in plasma dynamics.

It is noteworthy that the period during which the flux rope stays in its slow-rise “activation” phase may depend on the rope parameters. Eruptions with somewhat longer activation periods have been recently reported in the papers by Karlický and Kliem (2010), Kliem *et al.* (2010), and Kumar *et al.* (2012). In those cases quite a high winding number has led to an instability, resulting in a larger twist motion rather than to the rise of the flux rope. Thus, the actual motion pattern at the beginning of eruption (rather twisting or rather rising) probably depends on the model parameters used, *i.e.*, the winding number N_t and the rate with which the stabilizing field above the rope decays with height.

In Section 4.1 we used the results of the MHD simulations – the velocity field and the density distribution – as an input for a qualitative estimation of the H α emission. In order to compare the model results with observations and thus address the question of whether the initial phase of the flux rope eruption can account for observed data, we calculated the modeled filtergram image and spectral line profile along the simulated slit of the spectrograph. The modeled and observed data are qualitatively similar; compare Figures 4 and 9. We used very simplified assumptions for the emission calculation. Nevertheless, we still believe that robust characteristics of the spectral line like those we compared here (the central wavelength and the line width) are not overly dependent on the details of radiative transfer modeling (unlike some more detailed properties of lines, *e.g.*, asymmetry or self-absorption in a line core; see, *e.g.*, Heinzel and Anzer, 2001, and references therein).

In some cases we observe clearly varying Doppler shifts along the spectrograph slit, resulting in a tilted distribution of the emission-line profile along the slit. This is clearly visible in Figures 4 and 10a and in line with our modeled emission in Figure 9. Similar effects (mostly in their initial phases) can also be seen in other studied limb events. In addition to the line-center shift one can also observe significant broadening of the line. This is partly due to the internal motions inside the flux rope along the LOS – either regular (*e.g.*, torsional or helical) motion of the plasmas, or that caused by the plasma turbulence. Nevertheless, nonideal observing conditions (seeing) also contribute to the line broadenings as the atmospheric turbulence brings and mixes the radiation from places with different LOS velocity to the same position on the slit. We took all these effects into account when introducing the microturbulent velocity v_T in Equation (14).

However, sometimes only strong line broadening is observed without any significant shift of the line center, as in Figure 2. This occurs in later stages of the limb event, in our case at 09:05:46 UT. A possible interpretation of this observation is perhaps the internal motions in the knot that can be seen in the loop top of the bottom flux rope in Figure 4 in the simulations by Ozaki and Sato (1997). Due to the high twisting number even reconnection can start in this knot; a similar feature has been observed in Kliem *et al.* (2010). The counterstreaming reconnection outflows might be responsible for “static” (*i.e.*, without significant line-center Doppler shift) spectral line broadening. Alternatively, similar reconnection outflows might also be caused by the reconnection between the rotating flux rope and the surrounding magnetic field. An indication that a weaker reconnection (and particle acceleration) process already takes place in this preimpulsive phase is provided by the decimetric type III burst in the radio spectrum (Figure 7) at 09:04 UT. Nevertheless, this possible reconnection event is out of the scope of our model, which focuses on the very initial phase only.

To sum up, the MHD model and its extension, providing emulated image and spectral data, support the working hypothesis, which interprets the observed event in terms of macroscopic motions during the very initial phase of the flux rope eruption. Nevertheless, a question arises: To what extent is the model’s final outcome – *i.e.*, the calculated filtergram and spectrum – sensitive to the underlying MHD model? We address this issue in the next subsection.

5.1. Testing Model Sensitivity: Kinematic Models of Plasma Flows

In order to test the sensitivity of the modeled H α data (the rather low-resolved filtergram and spectrum along the slit) to changes in the underlying model of the flow pattern and density distribution, we performed a set of purely kinematic models of plasma flows. In this class of models various analytically described bodies like a cylinder, a cone, a sphere, or a helical tube are populated by various plasma flow patterns either on the surfaces or in the volume of the model bodies. Then, after selecting a viewing angle (LOS) and position of the simulated spectrograph slit (similarly as in Section 4.1), the modeled filtergram and spectrum are calculated. The procedure of emission calculation is a bit more complicated compared with the case described in Section 4.1, and it includes a simple integration of the radiative transfer equation. For details about the procedure and kinematic modeling in general, see Havlíčková and Kotrč (2006) and Karlický, Kotrč, and Kupryakov (2001).

Running the kinematic models with subsequent emission calculations for various selected bodies and flow patterns results in a grid of image+spectrum models, from which one model, whose results best reproduce the observations, can be selected. We have found that the observed data are best fitted by the model of plasma flowing through the helical tube. The results are shown in Figure 10. Panels (a), (b), (c), and (d) show, respectively, the

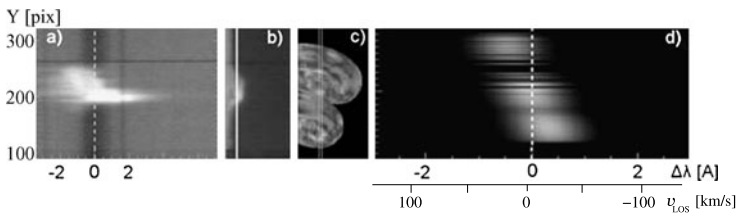


Figure 10 Kinematic modeling of the 4 August 2002 event. The model that best fits the observation uses plasma flowing through a single helical tube with two turns. (a) Observed $H\alpha$ spectrum along the slit 09:00:33 UT. Vertical dashed line corresponds to the spectral-line center in the rest frame. (b) Simultaneously taken slit-jaw $H\alpha$ filtergram. (c) Filtergram calculated from the above-mentioned underlying kinematic flow model. (d) Modeled spectral line for the same kinematic model of plasma flow.

observed $H\alpha$ spectrum along the slit, the corresponding slit-jaw image in the $H\alpha$ filter, the modeled slit-jaw image for plasma flowing through the helical tube, and the modeled spectrum along the emulated spectrograph slit, whose position is marked by a thin vertical line in panel (c). Unfortunately, the rather low spatial resolution of our observing instrument prevents a more detailed comparison of the modeled and observed $H\alpha$ filtergrams in panels (b) and (c). However, within these constraints the modeled and observed data fit qualitatively quite well.

The results of the kinematic modeling show that the flow pattern and plasma distribution resulting from the MHD model of the initial phase of flux rope eruption are not the only processes that could produce the observed structures in $H\alpha$. Nevertheless, the kinematic flow pattern that fits the observations best has some common properties with those from the MHD model; namely, both flows are constrained by some “helical guides.” From the dynamical point of view, basically two possibilities come into consideration: (i) the twisting (or de-twisting, in the case of already developed instability) motions during the initial phase of helical flux rope eruption studied in the current paper, and (ii) the plasma (*e.g.*, siphon) flow along the twisted magnetic field lines. However, related observations of the studied 4 August 2002 event, which show a subsequent CME formation originating in the same active region (Figure 5), favor the first possibility, when the standard scenario for solar eruptions and CMEs is taken into account.

5.2. Plasma Diagnostics Based on the Model

If we accept the interpretation of the 4 August 2002 limb event presented here, a knowledge of the driver of the observed plasma dynamics enables us to estimate some parameters that are usually hard to measure directly, such as Alfvén velocity and, consequently, the plasma beta parameter inside the prominence at the beginning of its eruption. In particular, the MHD model allows for the estimation of LOS velocities in terms of internal Alfvén speed inside the rope. As can be seen in Figure 9b, the maximum projection of the plasma velocity on the LOS during the confined phase of the eruption (*i.e.*, before the structure starts rising significantly) is $v_{\text{LOS}} \approx 0.1 V_{\text{A},0}$. If we compare this value with that observed by the spectrograph (Figure 4c), which gives $v_{\text{LOS,observ}} = 70 \text{ km s}^{-1}$, we obtain for the internal Alfvén speed inside the rope the value

$$V_{\text{A,int}} \approx 700 \text{ km s}^{-1}.$$

Now, the Alfvén velocity can be in a partly ionized hydrogen plasma related to the plasma beta parameter as follows:

$$\beta = \frac{n_{\text{tot}} k_B T}{B^2 / (2\mu_0)} = \frac{2(i+1)\rho k_B T \mu_0}{m_p B^2} = 2(i+1) \frac{k_B T}{V_A^2 m_p}, \quad (18)$$

where $n_{\text{tot}} = n_e + n_p + n_H$ is the total concentration of all species (electrons, protons, and neutral hydrogen atoms, respectively), and $i = n_p / (n_p + n_H)$ is the ionization degree. The simple fact that the structure is clearly visible in the H α line indicates that the temperature is not too high. Hence, taking plausible values for prominences $T = 10^4$ K, $i = 0.5$, and the Alfvén speed estimated above, we estimate

$$\beta \approx 5 \times 10^{-4}$$

for the active region prominence. Clearly, this procedure is sensitive to the estimation of what fraction of the Alfvén speed is actually projected on the LOS direction. This can depend on the MHD model parameters. We plan to make a parametric study of this question in our future work.

6. Conclusions

A correlation analysis of high-cadence H α FWHM time profiles with radio and SXR fluxes, in the course of studied solar flares, reveals a distinct type of spectroscopical observations which exhibit an unusual timing of the H α line broadening. Observations in this class do not fit the traditional view of line broadening as a chromospheric response to particle beam bombardment; hence, a different interpretation should be sought. In this paper we have studied in more detail a particular case of such an event that occurred on 4 August 2002. Based on the synthesis of collected related multiwavelength observations, we suggest an interpretation of the observed data in terms of macroscopic motions during the initial phase of flux rope eruption. We incorporated this hypothesis into a numerical MHD model. Starting from the Titov–Démoulin (1999) magnetic configuration filled by plasmas, we simulated the initial phase of the flux rope motion driven by the vortex boundary flows. The model results were recalculated in a form directly comparable with observations. The simulated and observed H α emissions (filtergrams and spectra) are qualitatively similar. Subsequent kinematic modeling of the spectroscopical response to various arbitrary patterns of plasma flows has indicated that – no matter what the driving force – the flow should be constrained by some helical guide in order to fit the observations. The flow driven by the twisting of the helical flux rope at the beginning of its eruption naturally conforms to this constraint, and it is the preferred one among other possibilities, as it is in line with the standard eruption scenario. It is also supported by the later observation of a CME originating in the investigated active region. Based on the model of the studied event, a diagnostic tool has been suggested that enables one to estimate the plasma beta parameter in the observed erupting prominence.

Acknowledgements We are very grateful to the anonymous referee for his/her valuable suggestions, which have improved the quality of the paper. We are also grateful to the SOHO instruments teams for providing free access to their results. This research was supported by a Marie Curie FP7-Reintegration Grant within the 7th European Community Framework Programme PCIG-GA-2011, project no. 304265 (SERAF). The work was further supported by grants GACR Nos. 205/09/1705, 205/09/1469, P209/10/1706, P209/10/1680, P209/12/1652, and P209/12/0103, and the research project RVO:67985815. The research leading to these results has received funding from the People Programme (Marie Curie Actions) of the European Union's Seventh Framework Programme FP7/2007-2013 under REA grant agreement no. 295272 (RADIOSUN).

References

- Bárta, M., Karlický, M., Žemlička, R.: 2008, Plasmoid dynamics in flare reconnection and the frequency drift of the drifting pulsating structure. *Solar Phys.* **253**, 173–189. doi:[10.1007/s11207-008-9217-5](https://doi.org/10.1007/s11207-008-9217-5).
- Bárta, M., Vršnak, B., Karlický, M.: 2008, Dynamics of plasmoids formed by the current sheet tearing. *Astron. Astrophys.* **477**, 649–655. doi:[10.1051/0004-6361/20078266](https://doi.org/10.1051/0004-6361/20078266).
- Bárta, M., Büchner, J., Karlický, M., Skála, J.: 2011a, Spontaneous current-layer fragmentation and cascading reconnection in solar flares. I. Model and analysis. *Astrophys. J.* **737**, 24. doi:[10.1088/0004-637X/737/1/24](https://doi.org/10.1088/0004-637X/737/1/24).
- Bárta, M., Büchner, J., Karlický, M., Kotrč, P.: 2011b, Spontaneous current-layer fragmentation and cascading reconnection in solar flares. II. Relation to observations. *Astrophys. J.* **730**, 47. doi:[10.1088/0004-637X/730/1/47](https://doi.org/10.1088/0004-637X/730/1/47).
- Battaglia, M., Fletcher, L., Benz, A.O.: 2009, Observations of conduction driven evaporation in the early rise phase of solar flares. *Astron. Astrophys.* **498**, 891–900. doi:[10.1051/0004-6361/200811196](https://doi.org/10.1051/0004-6361/200811196).
- Gunár, S., Heinzel, P., Anzer, U.: 2011, Synthetic differential emission measure curves of prominence fine structures. *Astron. Astrophys.* **528**, A47. doi:[10.1051/0004-6361/201015957](https://doi.org/10.1051/0004-6361/201015957).
- Havlíčková, E., Kotrč, P.: 2006, Spectra and models of prominence mass motion. *Cent. Eur. Astrophys. Bull.* **30**, 43–53.
- Heinzel, P., Anzer, U.: 2001, Prominence fine structures in a magnetic equilibrium: two-dimensional models with multilevel radiative transfer. *Astron. Astrophys.* **375**, 1082–1090. doi:[10.1051/0004-6361:20010926](https://doi.org/10.1051/0004-6361:20010926).
- Karlický, M., Bárta, M.: 2011, Successive merging of plasmoids and fragmentation in a flare current sheet and their X-ray and radio signatures. *Astrophys. J.* **733**, 107. doi:[10.1088/0004-637X/733/2/107](https://doi.org/10.1088/0004-637X/733/2/107).
- Karlický, M., Kliem, B.: 2010, Reconnection of a kinking flux rope triggering the ejection of a microwave and hard X-ray source I. Observations and interpretation. *Solar Phys.* **266**, 71–89. doi:[10.1007/s11207-010-9606-4](https://doi.org/10.1007/s11207-010-9606-4).
- Karlický, M., Kotrč, P., Kupryakov, Y.A.: 2001, Axially-symmetric velocities in the 15 May 2000 eruptive prominence. *Solar Phys.* **199**, 145–155.
- Kliem, B., Török, T.: 2006, Torus instability. *Phys. Rev. Lett.* **96**(25), 255002. doi:[10.1103/PhysRevLett.96.255002](https://doi.org/10.1103/PhysRevLett.96.255002).
- Kliem, B., Karlický, M., Benz, A.O.: 2000, Solar flare radio pulsations as a signature of dynamic magnetic reconnection. *Astron. Astrophys.* **360**, 715–728.
- Kliem, B., Linton, M.G., Török, T., Karlický, M.: 2010, Reconnection of a kinking flux rope triggering the ejection of a microwave and hard X-ray source II. Numerical modeling. *Solar Phys.* **266**, 91–107. doi:[10.1007/s11207-010-9609-1](https://doi.org/10.1007/s11207-010-9609-1).
- Kotrč, P.: 1997, Video cameras in the Ondrejov flare spectrograph – results and prospects. *Hvar Obs. Bull.* **21**, 97–108.
- Kumar, P., Cho, K.-S., Bong, S.-C., Park, S.-H., Kim, Y.H.: 2012, Initiation of coronal mass ejection and associated flare caused by helical kink instability observed by SDO/AIA. *Astrophys. J.* **746**, 67. doi:[10.1088/0004-637X/746/1/67](https://doi.org/10.1088/0004-637X/746/1/67).
- Lin, J., Forbes, T.G.: 2000, Effects of reconnection on the coronal mass ejection process. *J. Geophys. Res.* **105**, 2375–2392. doi:[10.1029/1999JA900477](https://doi.org/10.1029/1999JA900477).
- Magara, T., Mineshige, S., Yokoyama, T., Shibata, K.: 1996, Numerical simulation of magnetic reconnection in eruptive flares. *Astrophys. J.* **466**, 1054–1066. doi:[10.1086/177575](https://doi.org/10.1086/177575).
- Ozaki, M., Sato, T.: 1997, Interactions of convecting magnetic loops and arcades. *Astrophys. J.* **481**, 524. doi:[10.1086/304036](https://doi.org/10.1086/304036).
- Priest, E.R.: 1984, *Solar Magneto-Hydrodynamics, Geophysics and Astrophysics Monographs*, Reidel, Dordrecht.
- Shibata, K., Tanuma, S.: 2001, Plasmoid-induced-reconnection and fractal reconnection. *Earth Planets Space* **53**, 473–482.
- Švestka, Z.: 1976, *Solar Flares*. Springer, Berlin.
- Švestka, Z., Fritsová, L.: 1956, The width of H_{α} in solar flares. *Bull. Astron. Inst. Czechoslov.* **7**, 30.
- Titov, V.S., Démoulin, P.: 1999, Basic topology of twisted magnetic configurations in solar flares. *Astron. Astrophys.* **351**, 707–720.
- Török, T., Kliem, B.: 2005, Confined and ejective eruptions of kink-unstable flux ropes. *Astrophys. J. Lett.* **630**, L97–L100. doi:[10.1086/462412](https://doi.org/10.1086/462412).
- Valníček, B., Letfus, V., Blaha, M., Švestka, Z., Seidl, Z.: 1959, The flare spectrograph at Ondřejov. *Bull. Astron. Inst. Czechoslov.* **10**, 149.
- Williams, D.R., Török, T., Démoulin, P., van Driel-Gesztelyi, L., Kliem, B.: 2005, Eruption of a kink-unstable filament in NOAA active region 10696. *Astrophys. J. Lett.* **628**, L163–L166. doi:[10.1086/432910](https://doi.org/10.1086/432910).